INVESTIGATION OF MACROSEGREGATION FORMATION IN ALUMINIUM DC CASTING FOR DIFFERENT ALLOY SYSTEMS

Akash Pakanati[1], Mohammed M'Hamdi[1,2], Hervé Combeau[3,4], Miha Založnik[3,4]

[1] Dept. of Materials Technology, NTNU, N-7491 Trondheim, Norway
[2] SINTEF Materials and Chemistry, N-0314 Oslo, Norway
[3] Institut Jean Lamour, CNRS – Université de Lorraine, Campus Artem, 2 allée André Guinier, F-54000 Nancy, France
[4] Laboratory of Excellence on Design of Alloy Metals for low-mAss Structures ('DAMAS'), Université de Lorraine, France

* Corresponding author : Akash Pakanati (akash.pakanati@ntnu.no)

Abstract

Direct Chill (DC) Casting of Aluminium involves alloys employing different solute elements. In this paper a qualitative analysis and comparison of macrosegregation formation is presented for three different alloy systems: Al-Mg, Al-Zn and Al-Cu. For this purpose, a multiphase, multiscale solidification model based on volume averaging method accounting for shrinkage induced flow, thermal-solutal convection and grain motion is used and applied to an industrial scale DC Cast ingot. The primary difference between these alloys is thermal-solutal convection with Al-Mg having a competing thermal and solutal convection whereas the other two systems have a co-operating thermal and solutal convection. In the study, the combined effect of the macrosegregation mechanisms is analyzed for each alloy in order to assess the role of the alloy system on the final macrosegregation.

Keywords: Macrosegregation, Solidification, DC-Casting

1. Introduction

The redistribution of solute at the scale of cast product due to relative motion between solid and liquid phase is referred to as macrosegregation. This relative motion is driven by shrinkage induced flow, natural convection due to thermal and solutal gradients, movement of the equiaxed grains and thermally induced deformations of the mushy zone. A rather comprehensive description of these mechanisms can be found in literature[1].

Due the severity of this casting defect, a significant effort has been dedicated to to understanding and modelling of macrosegregation formation in DC casting. A study on the effect of shrinkage induced flow and thermal-solutal convection in DC Casting was made by Reddy and Beckermann[2] which was based on volume averaging method proposed by Ni and Beckermann[3]. Reddy and Beckermann studied Al-Cu billet and controlled natural convection intensity with the mushy zone permeability. For a moderately permeable mush, they observed positive segregation at the center and negative segregation close to the surface. Significant improvements in modeling has been achieved over the years, especially pertaining to grain motion. Wang and Beckermann[4,5] proposed the first model to numerically simulate equiaxed dendritic solidification in the presence of natural convection. Vreeman and Incropera[6,7] conducted a study on DC cast billets with Al-Mg and Al-Cu. Their model accounted for grain motion and thermal-solutal convection. Several recent advances were made in modelling of solidification[8–14] and dc casting process[15–23]. Založnik and Combeau[12] proposed an operator splitting scheme to couple macroscopic transport and grain growth in a two phase multiscale solidification model. The model was further extended to include inoculant motion[16,24].

52 Založnik et al[16]. conducted a systematic study of influence of various transport mechanisms
53 contributing to macrosegregation in an Al-Zn system. For a case with only thermal-solutal convection
54 as driving force, they also observed positive segregation at the center and negative segregation at the
55 surface respectively. This pattern was attributed to both copper and zinc being heavier than
56 aluminium resulting in contributing thermal and solutal convection. In contrast, Jalanti[25] and
57 Bedel[18] both independently concluded that the thermal-solutal convection in DC Casting of Al-Mg
58 contribute to negligible macrosegregation. Magnesium being lighter than aluminium results in
59 competing thermal-solutal convection.
60
61 In the current paper a two-phase, multiscale solidification model in which shrinkage induced flow,
62 natural convection, grain transport, heat transfer, solute transport and grain growth based on Založnik
63 and Combeau[12] and Tveito et al[24] is used to study macrosegregation formation in three binary
64 alloys: Al-Mg, Al-Zn and Al-Cu. The goal of this paper is to assess the impact of alloying element, if
65 any, on transport mechanisms which inturn affect the macrosegregation formation.
66
67 **2. Numerical Model**
68
69 The two-phase, multiscale numerical model used is based on the splitting method[12]. For a detailed
70 description of the model the reader is referred to the paper. Only the main features are described here
71 and the system of equations are summarized in Table 1 followed by description of the terms in Table
72 2. The Euler-Euler volume-averaged model considers macroscopic transport and microscopic growth.
73
74 The two-phase macroscopic transport accounts for heat, mass and solute transport coupled to phase
75 momentum transfer accounting for liquid flow induced by shrinkage, thermal-solutal convection and
76 grain motion. The density of liquid and solid are assumed to be constant but different and the
77 Bousinessq approximation is used for the liquid density in the buoyancy term. For the solid phase,
78 two flow regimes are considered depending on the solid fraction (g_s). For solid fractions lower than
79 packing fractions (g_{pack}) the solid (equiaxed globular grains) is freely floating. The interfacial drag
80 term C_D in Equation (8) is modeled in the same manner as Ref[12] for spherical particles. For solid
81 fractions greater than packing fractions, grains are assumed to form a rigid porous solid matrix
82 moving with the casting velocity, $\vec{V}_{cast}$. The interfacial drag now is modeled by a Darcy term, where
83 the permeability is calculated from the Kozeny Carman relation for the characteristic size, l_{KC}.
84
85 The microscopic part is treated locally within each control volume and accounts for both nucleation
86 and growth kinetics. Nucleation of grains is assumed to occur on grain-refiner (inoculant) particles.
87 According to the athermal nucleation theory of Greer et al[26], the critical undercooling for free growth
88 of a grain on an inoculant particle of diameter d is given by $\Delta T_c = 4\Gamma_{GT}/d$ where Γ_{GT} is the Gibbs-
89 Thompson coefficient. The number of activated particles then depends on the size distribution of the
90 particle population, which can be represented by an exponential distribution density function. This
91 representation holds for the largest particles, which are activated at small undercoolings and therefore
92 successful as nuclei. This size distribution is then discretized into m classes of inoculants. Each class i
93 is represented by a volumetric population density N_{nuc}^i and a critical undercooling ΔT_c^i . When the
94 local undercooling reaches the critical undercooling of class i, its local inoculant density, N_{nuc}^i, is
95 instantaneously added to the grain density, N_g, and N_{nuc}^i becomes locally zero. The conservation
96 equations for the density of each inoculant class and the grain density are shown in Equations (9) and
97 (10), respectively, where Φ^i represents the transfer of population density from inoculants to grains
98 upon nucleation. We assume grains nucleate on grain refiners and the morphology of the grain is
99 assumed to be globular. The model accounts for finite diffusion in both solid and liquid phases and
100 local thermal equilibrium is assumed.
101

Table 1: System of Equations

Macroscopic Conservation Equations

Averaged mass balance of liquid phase

$$\frac{d(g_l\rho_l)}{dt} + \nabla.(g_l\rho_l\vec{v}_l) = \Gamma_l \tag{1}$$

Averaged mass balance of solid phase

$$\frac{d(g_s\rho_s)}{dt} + \nabla.(g_s\rho_s\vec{v}_s) = \Gamma_s \tag{2}$$

Averaged solute balance of liquid phase

$$\frac{d(g_l\rho_l c_l)}{dt} + \nabla.(g_l\rho_l c_l\vec{v}_l) = \nabla.(g_l\rho_l D_l\nabla c_l) + c_l^*\Gamma_l + \frac{(S_v\rho_l D_l)}{\delta_l}(c_l^* - c_l) \tag{3}$$

Averaged solute balance of solid phase

$$\frac{d(g_s\rho_s c_s)}{dt} + \nabla.(g_s\rho_s c_s\vec{v}_s) = \nabla.(g_s\rho_s D_s\nabla c_s) + c_s^*\Gamma_s + \frac{(S_v\rho_s D_s)}{\delta_s}(c_s^* - c_s) \tag{4}$$

Averaged mixture enthalpy

$$\frac{d(\rho h_m)}{dt} + \nabla.(g_l\rho_l h_l\vec{v}_l + g_s\rho_s h_s\vec{v}_s) = \nabla.[(g_s k_s + g_l k_l)\nabla T] \tag{5}$$

Averaged liquid momentum

$$\frac{d(g_l\rho_l\vec{v}_l)}{dt} + \nabla.(g_l\rho_l\vec{v}_l\vec{v}_l) = -g_l\nabla p_l + \nabla.(g_l\mu_l\nabla\vec{v}_l) + g_l\rho_l\boldsymbol{g} + M_l^d \tag{6}$$

Averaged solid momentum

$$\begin{aligned} g_s < g_{pack}, \qquad 0 = -g_s\nabla p_l + g_s\rho_{s,b}\boldsymbol{g} - M_l^d \\ g_s > g_{pack}, \qquad \vec{v}_s = \vec{V}_{cast} \end{aligned} \tag{7}$$

Source term in momentum equation

$$M_l^d = \begin{cases} \dfrac{g_l^2\mu_l}{K}(\vec{v}_s - \vec{v}_l) & if\ g_s > g_{pack} \\ \dfrac{3g_s\rho_l C_D}{4(2R_s)}|\vec{v}_s - \vec{v}_l|(\vec{v}_s - \vec{v}_l) & if\ g_s < g_{pack} \end{cases} \tag{8}$$

Nucleation Modelling

Innoculant Motion

$$\frac{\partial}{\partial t}\left(N_{nuc}^i\right) + \nabla.\left(\vec{v}_l\, N_{nuc}^i\right) = -\Phi^i \tag{9}$$

Grain Population Balance

$$\frac{\partial}{\partial t}\left(N_g\right) + \nabla.\left(\vec{v}_s\, N_g\right) = \sum_{i=1}^{m}\Phi^i \tag{10}$$

Source term in nucleation modelling

$$\Phi^i = \begin{cases} N_{nuc}^i\, \partial(t) & ,\Delta T < \Delta T_c^i \\ 0 & , \qquad else \end{cases} ,i = 1,\dots,m \tag{11}$$

Microscopic Conservation Equations

Mass balance at solid-liquid interface

$$\Gamma_l + \Gamma_s = 0 \tag{12}$$

Solute balance at solid-liquid interface

$$(c_l^* - c_s^*)\Gamma_s = \frac{(S_v\rho_l D_l)}{\delta_l}(c_l^* - c_l) + \frac{(S_v\rho_s D_s)}{\delta_s}(c_s^* - c_s) \tag{13}$$

Diffusion lengths

$$\delta_s = \frac{R_s}{5} \tag{14}$$

$$\delta_l = min\left\{R_s\left(\frac{1}{1 - g_s^{1/3}} + \frac{Sc^{\frac{1}{3}}Re^{n(Re)}}{3(1 - g_s)}\right)^{-1}, R_s\right\} \tag{15}$$

where,

$$n(Re) = \frac{2Re^{0.28} + 4.65}{3(Re^{0.28} + 4.65)}, \ Re = \frac{\rho_l(1 - g_s)(2R_s)}{\mu_l}|\vec{v}_s - \vec{v}_l|$$

$$Sc = \frac{\mu_l}{\rho_l D_l}$$

Thermodynamic relations at solid-liquid interface	$c_s^* = k_p c_l^*$	(16)
	$T_{liq} = T_m + m_l c_l^*$	(17)

<u>Geometrical Relations</u>

Radius of the grain	$R_s = \left(\dfrac{3g_s}{4\pi N_g}\right)^{1/3}$	(18)
Interfacial area density of liquid-solid surface	$S_v = 4\pi(R_s)^2 N_g$	(19)

102

Table 2: Nomenculature

Symbol	Description	Symbol	Description
c	average mass concentration, wt. %	μ_l	liquid dynamic viscosity, Pas
g	volume fraction, -	N_{nuc}^i	innoculant density for class i, m^{-3}
t	time, s	N_g	grain density, m^{-3}
v	Intrinsic velocity, ms^{-1}	$\delta(t)$	Dirac function
K	permeability, m^2	ΔT	undercooling, °C
C_D	drag co-efficient, -	ΔT_c^i	critical undercooling for inoculant class i, °C
p_l	liquid pressure, Nm^{-2}	R_s	radius of the grain, m
Sc	Schmidts number		
Re	Reynolds number		
T_{liq}	temperature of liquidus, °C		
h_m	mixture enthalpy, Jkg^{-1}	*Greek Symbols*	
k	thermal conductivity, W/(mK)	Γ	growth rate
g	acceleration due to gravity, -9.81 m/s^2	Φ	solid mass generated due to nucleation
S_v	solid liquid interfacial area density, m^{-1}	δ	diffusion length
g_{pack}	packing fraction, -		
V_{cast}	cast velocity, mm/min	*Subscripts and Superscripts*	
$\rho_{s,b}$	solid buoyancy density, kgm^{-3}	l	liquid
T_m	melting temperature of pure Aluminium, °C	s	solid
m_l	liquidus slope, °C/ wt. %	$*$	solid-liquid interface

103
104

3. DC Casting Case Study
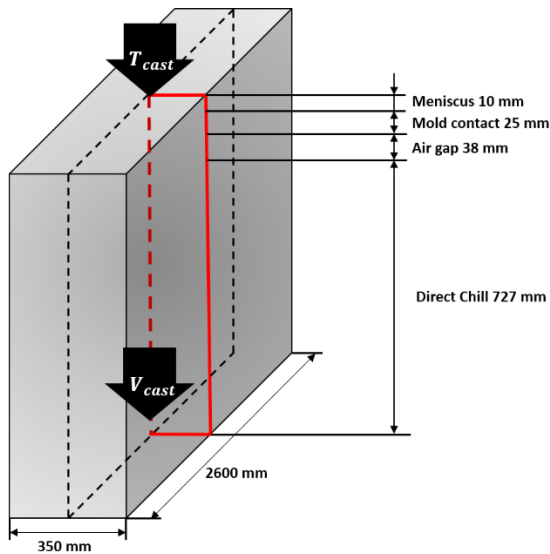

Figure 1: Ingot Geometry with corresponding boundary conditions given in Table 3
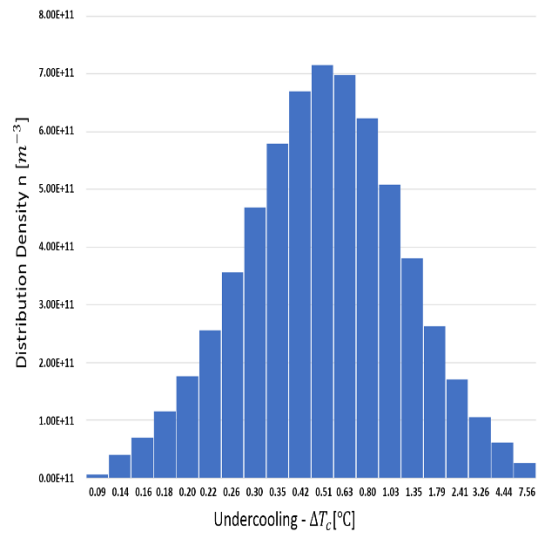

Figure 2: Innoculant Distribution

The DC Casting geometry is based on the case study performed by Založnik et al[16] with slightly different boundary conditions. An industrial scale ingot with thickenss of 350 mm is considered. The geometry is simplified to 2D and symmetry is assumed at the central axis. The schematics can be seen in Figure 1. The 2D slice marked in red represents the simulation domain and the dashed line indicates symmetry axis. Liquid metal maintained at casting temperature T_{cast}, reference solute concentration C_o and inoculant density N_{nuc}^i, enters the domain through the inlet at the top. The inlet velocity is calculated based on mass balance accounting for solidification shrinkage. The solidified metal leaves the domain from outlet at the bottom at predefined casting speed V_{cast} of 60mm/min and acceleration due to gravity, $\mathbf{g}$ = -9.81 m^2/s is in the vertical direction.. The primary and secondary cooling heat fluxes are modelled with Fourier condition ($q = h(T_{amb} - T)$). Primary cooling consists of three zones – meniscus, mold and air gap. The boundary conditions are specified in Table 3. The secondary cooling heat transfer coefficient is modelled by the correlation given by Weckmann and Niessen[27], as shown in Equation (20).

$$h_{secondary}(T) = \{A + B \cdot (T[\text{K}] + T_{water}[\text{K}])\} \cdot \left(\frac{Q_{water}}{P}\right)^{\frac{1}{3}} + C \cdot \frac{(T-T_{sat})^3}{T-T_{water}} \tag{20}$$

$$\text{Where } A = -167000 \ [\text{W}\cdot\text{s}^{\frac{1}{3}}\cdot\text{m}^{-8/3}];$$

$$B = 352 \ [\text{W}\cdot\text{s}^{1/3}\cdot\text{m}^{-8/3}\cdot\text{K}^{-1}]; \qquad C=20.8 \ [\text{W}\cdot\text{m}^{-2}\cdot\text{K}^{-2}]$$

Where $h_{Secondary}$ is the heat transfer coefficient, T is the surface temperature of the ingot, T_{water} is the water temperature, T_{sat} is the boiling temperature of the water, Q_{water} is the water flow rate per ingot, and P is the ingot perimeter. The values assumed for the variables in it are presented in Table 3.

The size distribution for inoculant particles taken from[28] for 2kg/ton of innoculants of type TiBi$_2$ is shown in Figure 2. The distribution density against the undercooling is plotted which increases to a maximum at around 0.5 °C and decreases. In this study, the inoculant distribution is discretized into

129 20 classes (m=20). The inoculant distribution considered here is inadequately characterized and
130 cannot be taken as accurate representation of realistic casting conditions for the different alloy
131 systems used. For the sake of simplicity, the distribution in Figure 2 will be used for the studied cases.
132
133
134

Table 3: Boundary Conditions for Energy, Liquid Momentum and Solid Momentum			
Boundary	Energy	Liquid Momentum	Solid Momentum
Inlet	$T_{cast} = 953.15$ K	calculated	-
Meniscus	$h = 1$ W/(m^{2}K) , $T_{amb} = 293.15$ K	Nonslip	Nonslip
Mold Contact	$h = 350$W/(m^{2}K) , $T_{amb} = 293.15$ K	Nonslip	Nonslip
Air Gap	$h = 50$ W/(m^{2}K) , $T_{amb} = 293.15$ K	Nonslip	Nonslip
Direct Chill	Based on Equation (20) $T_{water} = 293.15$ K, $T_{sat} = 373.15$ K, $Q_{water} = 20 \ l/min$	Nonslip	Nonslip
Outlet	-	-	V_{cast}

135
136 The thermophysical data for the different binary alloys are given in Table 4 which are based on the
137 data obtained from Jalanti[25] for Al-Mg and Al-Cu and from Založnik et al[16] for Al-Zn. The diffusion
138 co-efficients of solid and liquid for Al-Cu are obtained from Tveito et al[24] A linearized phase
139 diagram is assumed defined by the constant liquidus slope, partition coefficient and the pure melting
140 temperature. The liquid density is assumed to be constant in all terms except the buoyancy terms
141 invoking the Boussinesq approximation. The density of solid accounting for buoyancy effects in solid
142 momentum equation is assumed to be constant. The packing fraction is set at 0.3.
143
144 The transport equations are solved with a Finite Volume Method and the SIMPLE-algorithm for
145 staggered grid is used for pressure-velocity coupling. The convective terms are discretized with a
146 first-order upwind scheme and for time discretization a fully implicit first-order scheme is used. For
147 all simulations a structured grid of 16384 cells ($N_x \times N_y = 64 \times 256$) is employed. A constant time step of
148 0.02s is used and the calculations are run until steady state.
149
150

Table 4: Thermophysical Data Used in Numerical Simulations				
Property	**Unit**	**Al-Mg**[25]	**Al-Cu**[25]	**Al-Zn**[16]
Specific Heat (c_p)	$\text{J kg}^{-1}\text{K}^{-1}$	1107.0	1107.0	1300.0
Latent Heat (L)	J kg^{-1}	3.92e5	3.92e5	3.63e5
Solid Thermal Conductivity (k_s)	$\text{W m}^{-1}\text{K}^{-1}$	100.0	100.0	185.0
Liquid Thermal Conductivity (k_l)	$\text{W m}^{-1}\text{K}^{-1}$	100.0	100.0	75.0
Melting Temperature (T_m)	K	933.65	933.65	950.95
Eutectic Temperature (T_{eut})	K	723.15	821.35	750.7
Dynamic Viscosity (μ_l)	Pa s	1.2e-3	1.2e-3	1.28e-3
Solid Density (ρ_s)	Kg m^{-3}	2550	2550	2662.5
Liquid Density (ρ_l)	Kg m^{-3}	2400	2400	2519.0
Solid Buoyancy Density $(\rho_{s,b})$	Kg m^{-3}	2550	2550	2662.5
Thermal Expansion Co-efficient (β_T)	K^{-1}	1.245e-4	1.245e-4	1.5e-4
Solutal Explansion Co-efficient (β_C)	$(\text{wt\%})^{-1}$	4.0e-3	-1.09e-2	-1.23e-2
Characteristic Length for Permeability (l_{KC})	m	1.0e-4	1.0e-4	1.0e-4
Packing Fraction (g_{pack})	-	0.3	0.3	0.3
Reference Solute Concentration (C_o)	wt%	4.5	4.5	8.375
Partition Co-efficient (k_p)	-	0.485	0.173	0.257
Liquidus Slope (m_l)	$\text{K (wt\%)}^{-1}$	-5.831	-3.434	-6.05
Liquid Diffusion Co-efficient (D_l)	m^2s^{-1}	7.7e-9	3.8e-9	5.66e-9
Solid Diffusion Co-efficient (D_s)	m^2s^{-1}	1.8e-12	4.2e-13	5.60e-13

151
152

4. Results and Discussion

A brief overview of all the cases for each alloy system are summarized in Table 5. The study considers a total of five Cases (1-5) based on the driving mechanisms considered. Each case is further divided into *a,b,c* depending on the alloy used – magnesium (*a*), copper (*b*) and zinc (*c*). Cases 1-3 deal with individual transport mechanisms considering shrinkage induced flow (SH), natural convection (NC) and grain motion (GM), respectively. In Cases 1 and 2, a fixed solid velocity is employed by imposing $\langle \vec{v}_s \rangle^s = \vec{V}_{cast}$. Cases 4 and 5 deal with combinations. Case 4 is constructed by accounting for both natural convection and grain motion. Case 5 is constructed by adding shrinkage induced flow to Case 4. Macrosegregation plots overplotted with relative liquid velocity $(\vec{v}_l - \vec{V}_{cast})$ for Cases 1-5 are depicted in Figure 3 - Figure 5 and in Figure 8 and Figure 9. Relative segregation plotted against the cross-section of the ingot from center to surface for all the cases are show in Figure 6 and Figure 10 respectively.

Table 5: Simulation Cases				
Driving Mechanisms	Al-Mg	Al-Cu	Al-Zn	Description
Shrinkage Induced Flow (SH)	Case 1a	Case 1b	Case 1c	$g_{pack} = 0$ and $\beta_T = \beta_C = 0$
Natural Convection (NC)	Case 2a	Case 2b	Case 2c	$\rho_s = \rho_l$ and $g_{pack} = 0$
Grain Motion (GM)	Case 3a	Case 3b	Case 3c	$\rho_s = \rho_l$, $g_{pack} = 0.3$ and $\beta_T = \beta_C = 0$
Natural Convection (NC) and Grain Motion (GM)	Case 4a	Case 4b	Case 4c	$\rho_s = \rho_l$ and $g_{pack} = 0.3$
Natural Convection (NC) + Grain Motion (GM) + Shrinkage Induced Flow (SH)	Case 5a	Case 5b	Case 5c	$g_{pack} = 0.3$

4.1. Macrosegregation due to individual transport mechanisms

Figure 3 (a,b,c) shows the macrosegregation pattern for different alloys due to shrinkage induced flow. Flow is induced by pressure drop created to feed shrinkage. In the mushy zone, the velocity vectors are nearly perpendicular to the solid fraction iso-contours with significant deviations in flow direction close to the surface and center of the ingot where the shape (curvature) of the mush changes. The diverging flow pattern close to the center transports solute rich liquid away from center resulting in negative segregation. Slightly positive segregation in most part of cross section and positive segregation at the surface is observed similar to results in Ref[16]. The flow patterns observed in different alloy systems in Figure 3 are similar. Figure 6a show the relative segregation for the same cases and the curves are qualitiatively quite similar with some differences in the intensity and extent of the negative or positive segregation at the center and surface respectively.

For Case 2 (a,b,c) the driving force is natural convection (thermal-solutal) convection. Case 2a has a competing thermal and solutal convection whereas Case 2b and 2c have co-operating thermal and solutal convection. Thermal convection tends to set up clockwise flow loop as heavy cooled liquid descends along the inclined mushy zone and hotter liquid ascends in the center[16]. Solutal convection on the other hand can result in clockwise or counter clockwise flow loop depending on the alloying element being heavier or lighter than aluminium. Figure 4a shows the macrosegregation profile with

188   relative velocity vectors for Case 2a consisting of magnesium as the alloying element. Magnesium is
189   lighter than aluminium and results in a counter clockwise flow loop close to the center whereas the
190   rest of the liquid pool has a clockwise loop due to thermal convection. The overall macrosegregation
191   profile is a result of competition of thermal and solutal convection. This results in close to zero
192   relative macrosegregation as it can be seen in Figure 6b for Case 2a and it is quite similar to the ones
193   observed by Jalanti[25] and Bedel[18]. Figure 4b and Figure 4c show the macrosegregation profile for
194   Al-Cu and Al-Zn. Both copper and zinc are heavier than aluminium and result in a co-operting
195   thermal-solution convection. The flow pattern due to the clockwise loop is also quite similar for both
196   the cases. This results in negative segregation close to the surface as flow enters the mushy zone
197   satisfying the criterion $(\vec{v}_l - \vec{V}_{cast}).\nabla T < 0$[29]. Towards the center, flow leaves the mushy zone
198   resulting in positive segregation by satisfying the criterion $(\vec{v}_l - \vec{V}_{cast}).\nabla T > 0$. Figure 6b shows the
199   relative segregation for Cases 2b and 2c along with 2a. Qualitatively Al-Cu and Al-Zn exhibit similar
200   segregation behavior with differences in the intensity and together exhibit a strong contrast to Al-Mg.
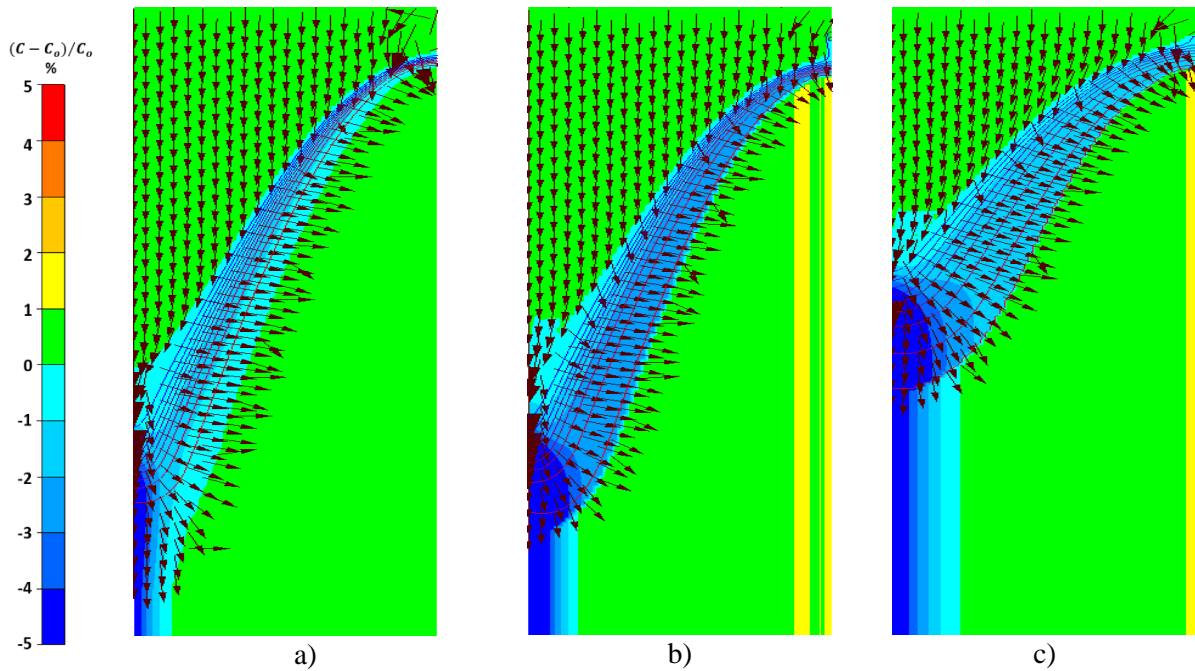201

Figure 3: Relative composition of Magnesium (a), Copper (b) and Zinc (c) in % and iso-lines of solid
fraction for Case 1a, 1b and 1c. Relative velocity $\vec{v}_l - \vec{V}_{cast}$ are also over plotted.

202
203   Figure 5 (a,b,c) shows macrosegregation pattern for Case 3(a,b,c). Grains are assumed to freely move
204   in the slurry region ($g_s < g_{pack}$). Grain transport affects the shape of the mush. Close to the surface,
205   cooling rate is high resulting in rapid growth of solid fraction resulting in a narrow slurry region.
206   Hence, the influence of grain motion is nonexistent in this region. Away from the surface, the cooling
207   rate reduces resulting in a larger region of the slurry zone. Macrosegregation formation due to grain
208   motion is primarily due to the settling of heavy solute lean grains along the inclined mushy zone
209   towards the center of the center resulting in negative segregation[16]. This accumulation of grains
210   results in expulsion of solute rich liquid upwards which causes an enrichment above the slurry zone.
211   The enriched liquid is carried into the liquid pool and then towards the mid-section of the ingot
212   resulting in positive segregation in the immediate vicinity of the center towards the surface. The flow
213   pattern due to grain settling shown in Figure 5 for different systems exhibit similar behavior and
214   consistent with relative segregation seen across the cross section shown in Figure 6c - negative
215   segregation in the center, positive segregation in the midsection and little to no segregation towards
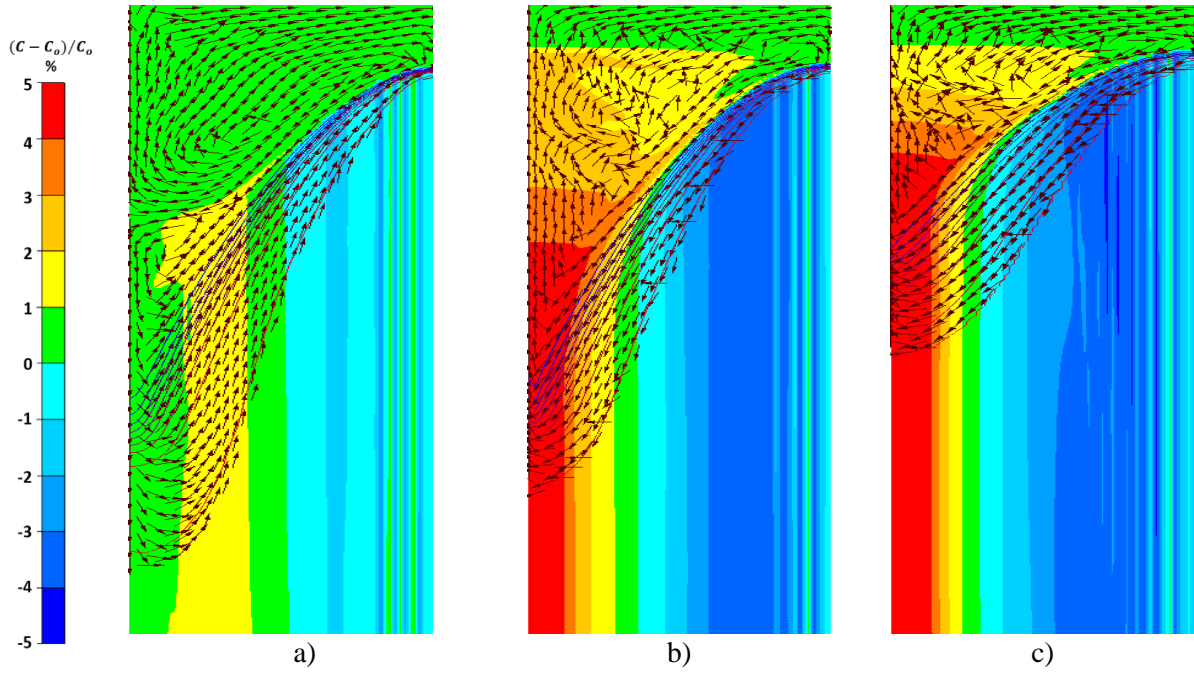216   the surface.
217

Figure 4: Relative composition of Magnesium (a), Copper (b) and Zinc (c) in % and iso-lines of solid fraction for Case 2a, 2b and 2c. Relative velocity $\vec{v}_l - \vec{V}_{cast}$ are also over plotted.
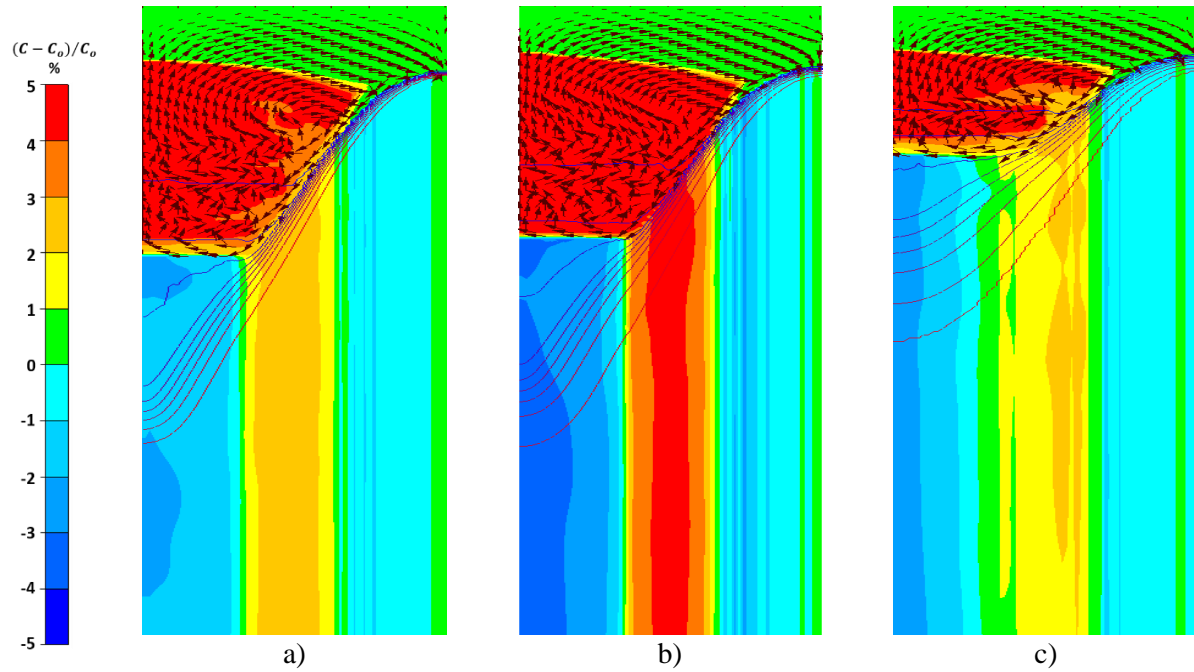

Figure 5: Relative composition of Magnesium (a), Copper (b) and Zinc (c) in % and iso-lines of solid fraction for Case 3a, 3b and 3c. Relative velocity $\vec{v}_l - \vec{V}_{cast}$ are also over plotted.

Figure 7 shows the grain diameter plotted across the cross section of the ingot for the different alloy systems for Case 3(a,b,c). All exhibit a similar trend of relatively uniform diameter with some fluctuations close to the surface. It can be seen that Case 3a and 3b have almost same grain structure whearease Case 3c exhibits smaller grain structure compared to the other two. This can be attributed to Growth Restriction Factor (GRF) given by $m_l(k_p - 1)C_o$. Grain diameter is inversely related to GRF[30]. Al-Zn (Case 3c) has GRF value of 37.6 whereas Al-Mg (Case 3a) and Al-Cu (Case 3b) have 13.5 and 12.7 respectively.
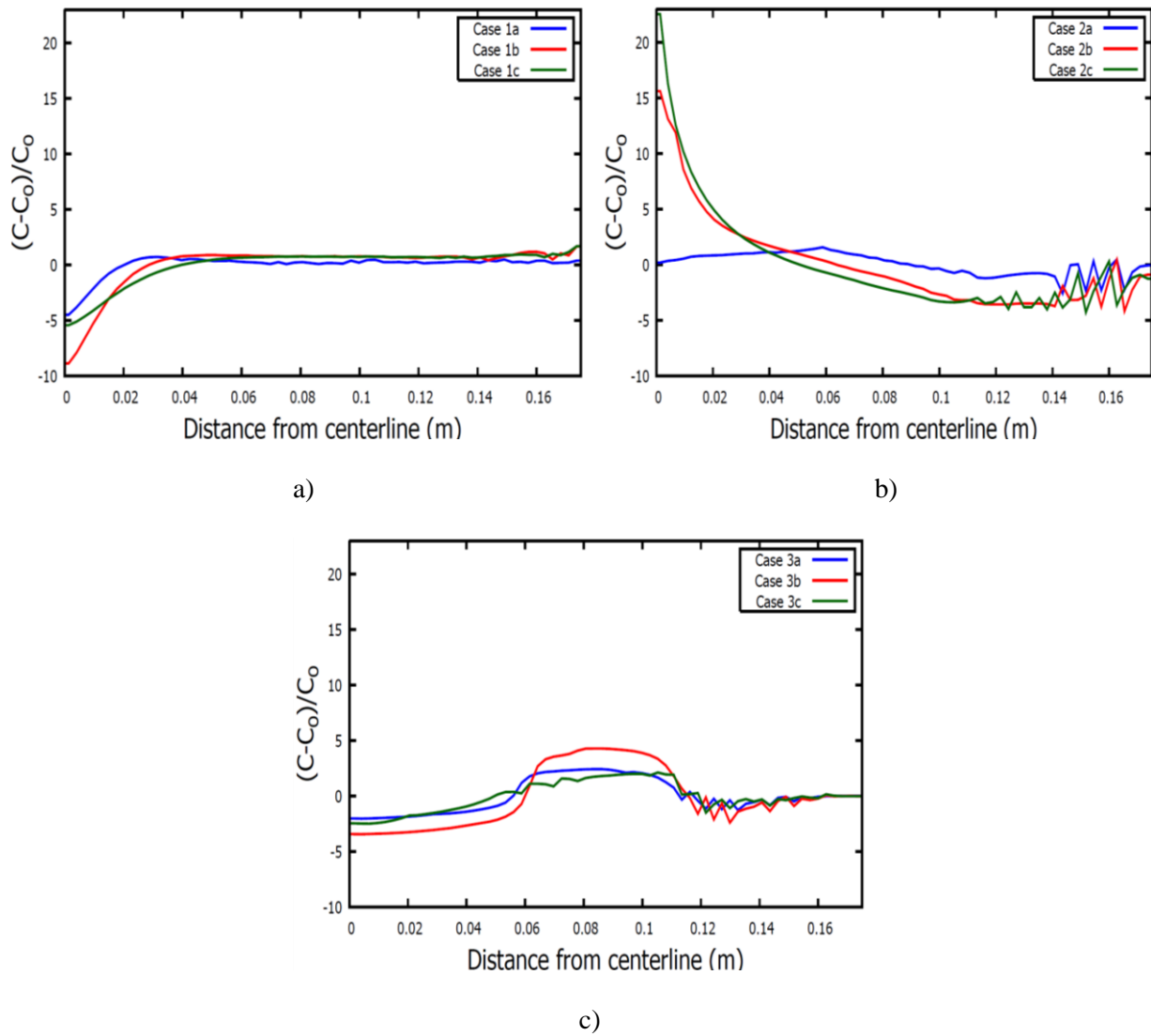
a)

b)

c)

Figure 6: Horizontal relative segregation profiles of the ingot for a) Cases 1, b) Case 2 and c) Case3 and case notation *a,b* and *c* indicate Al-Mg, Al-Cu and Al-Zn respectively
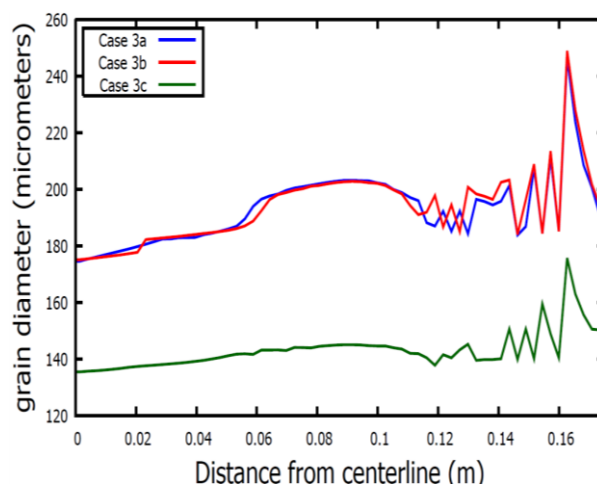

Figure 7: Horizontal profile of grain diameter of the ingot for Case 3 (Grain Motion only) and case notation *a,b* and *c* indicate Al-Mg, Al-Cu and Al-Zn respectively.

227
228

11

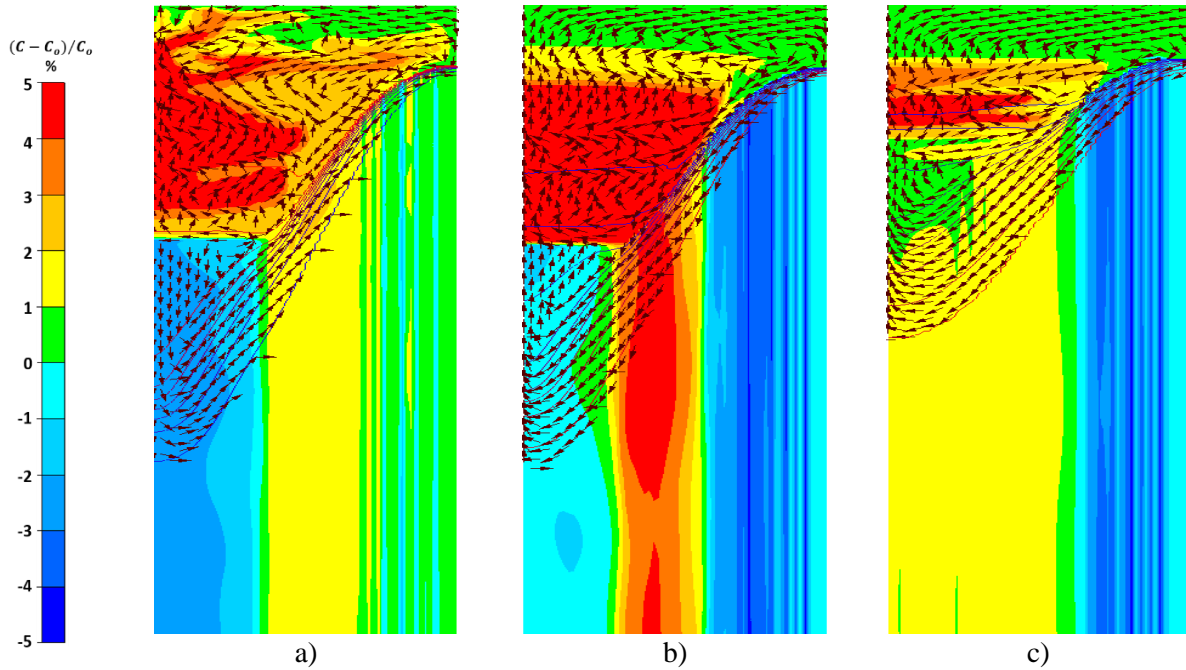229 *4.2. Macrosegregation due to combined transport mechanisms*
230

Figure 8: Relative composition of Magnesium (a), Copper (b) and Zinc (c) in % and iso-lines of solid fraction for Case 4a, 4b and 4c. Relative velocity $\vec{v}_l - \vec{V}_{cast}$ are also over plotted.
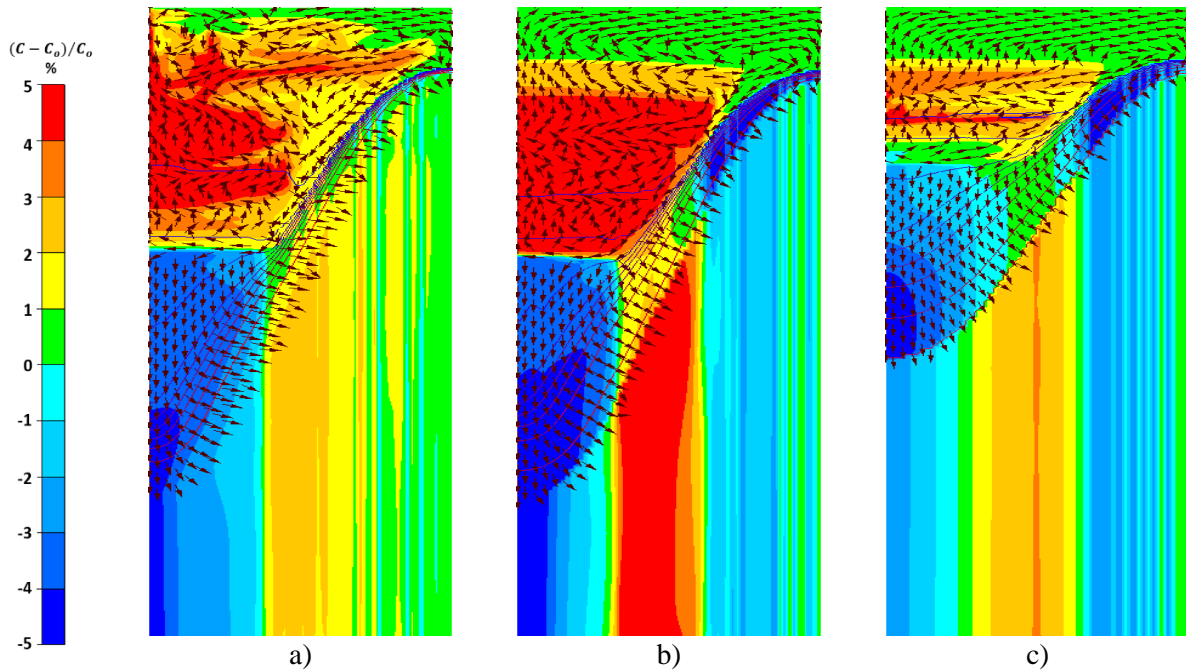
231
232

Figure 9: Relative composition of Magnesium (a), Copper (b) and Zinc (c) in % and iso-lines of solid fraction for Case 5a, 5b and 5c. Relative velocity $\vec{v}_l - \vec{V}_{cast}$ are also over plotted.

233
234 Case 4 (a,b,c) has combined phenomea of grain motion and natural convection. The macrosegregation
235 plots are shown in Figure 8. Case 4b and Case 4c exhibit similar flow pattern. Close to the surface due
236 to high cooling rates and thin slurry region, natural convection is driving cause for macrosegregation
237 and this results in negative segregation as flow enters the mushy zone. Due to co-operating thermal
238 and solutal convection, the flow loop is in the same direction as grain settling towards the center of

12

239   the ingot. This reduces the relative velocity between liquid and solid resulting in lowered settling
240   velocities of solid grains. Due to this, reduced negative intensity for Case 4b and slightly positive
241   segregation for Case 4c is observed (Figure 10a). These slight differences could be attributed to
242   differences in solid to liquid density ratios for copper and zinc. Similar patterns for zinc are observed
243   by Založnik et al[16]. The same discussion cannot be held for Case 4a which has a different natural
244   convection profile. When we refer to Figure 4a, natural convection individually results in two
245   convective loops for Al-Mg – clockwise in the liquid pool due to thermal effects and counter
246   clockwise close to the center of the ingot and mushy zone due to solutal effects. This breaking of flow
247   loops has little to no impact on the grain settling. The relative velocity is not reduced and grains
248   settling leads to more negative segregation when compared with Al-Cu or Al-Zn. Infact if we compare
249   Figure 6c (grain motion only) and Figure 10a (grain motion with natural convection) for Al-Mg, the
250   relative segregation profiles remain largely same, especially in the center and mid-section. The
251   coupling of grain motion and natural convection also results in slightly different flow pattern for Case
252   4a as can seen in Figure 8a when compared with Case 4b and 4c in Figure 8b Figure 8c
253   respectively.The flow pattern in the slurry and liquid zone at the center of the ingot in Figure 8a
254   shows expulsed solute due to grain settling rising towards the inlet (Mg is lighter than Al). This solute
255   meets the incoming solute from the inlet and could lead to turbulent behavior, a phenomena which
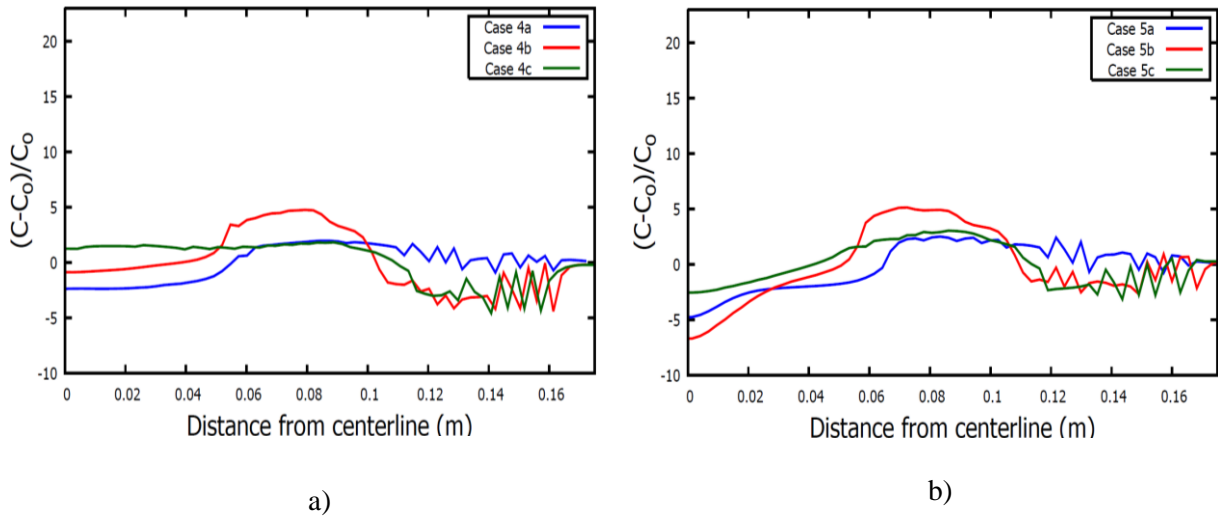256   was also mentioned by Vreeman and Incropera[7].
257

Figure 10: Horizontal relative segregation profiles of the ingot for a) Cases 4 and b) Case 5 and case notation *a,b* and *c* indicate Al-Mg, Al-Cu and Al-Zn respectively.

258
259   Case 5 is an extension of Case 4 with additional effect of shrinkage induced flow which acts at higher
260   solid fraction regions where the effects of grain motion and natural convection are negligible. The
261   shape of the mushy zone changes due to grain motion and this affects the shrinkage induced flow as
262   described in Ref[16] but shrinkage induced flow does not have any impact on grain motion or natural
263   convection. This one way coupling does not change the flow pattern in slurry and liquid regions
264   which can be observed when we compare Figure 9 with Figure 8. This reasoning holds well for all the
265   three alloy systems. Figure 10b shows the relative segregation profiles across the cross section of the
266   ingot for all three alloy systems. These profiles are quite similar to the ones observed in the
267   experiments[31]. All the three predict negative segregation at the center followed by positive
268   segregation in the mid section. A slightly negative (copper and zinc) to positive segregation
269   (magnesium) close to the surface and a slightly positive segregation at the surface. The contribution to
270   negative segregation at the center changes with the alloy system and can be seen in Figure 11, which
271   has the vertical relative segregation profiles on the x axis and vertical distance from the bottom of the
272   ingot on the y axis. Al-Mg with cases 4a (GM+NC) and 5a (GM+NC+SH) is plotted in Figure 11a.

Case 4a already predicts ca -2.5% negative segregation at the center and addition of shrinkage induced flow doubles this value. Almost zero (Figure 11b) and slightly positive (Figure 11c) segregation is predicted by Al-Cu and Al-Zn respectively when shrinkage induced flow is not considered. Analysis indiciates that the combined effect of natural convection and grain motion on centerline segregation for Al-Cu and Al-Zn is minimum. Thereby revealing the significant negative segregation induced by shrinkage induced flow at the center of the ingot[7].
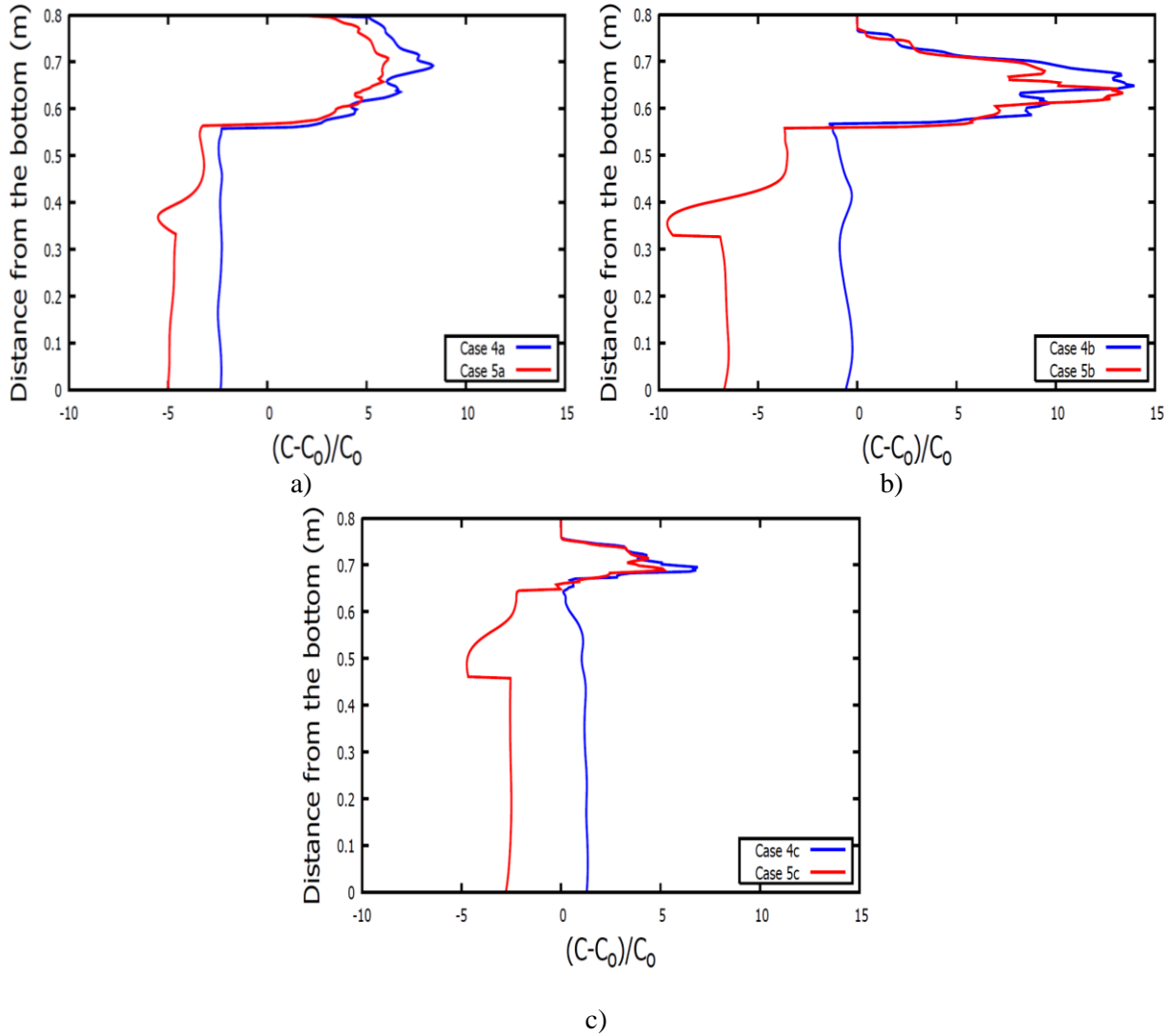

Figure 11: Vertical relative segregation profiles of the ingot for Cases 4 (GM+NC) and 5 (GM+NC+SH) for each alloy: a) Magnesium, b) Copper and c) Zinc

Table 6: Relative centerline segregation for different cases (measured in %)			
Cases (Transport Mechanisms)	Al-Mg (*a*)	Al-Cu (*b*)	Al-Zn (*c*)
Case 1 (SH)	-4.5	-8.8	-5.4
Case 2 (NC)	0.2	15.5	22.5
Case 3 (GM)	-2	-3.4	-2.5
Case 4 (NC+GM)	-2.5	-0.9	1.2
Case 5 (NC+GM+SH)	-4.7	-6.7	-2.5

282 In Table 6, we have summarized the relative macrosegregation values (in %) at the center of the ingot
283 for the different binary alloys and transport mechanisms considered in this study. For Al-Mg binary
284 alloy, shrinkage induced flow and grain motion taken separately result in negative segregation
285 whereas natural convection results in almost no segregation. The weak natural convection barely
286 affects the grain settling and as a consequence, combining grain motion and natural convection does
287 not affect the negative segregation. By including shrinkage induced flow, we further deplete solute
288 elements at the center of the ingot. For Al-Cu binary alloy, shrinkage induced flow and grain motion
289 when considered separately, also result in negative segregation as in the case of Al-Mg binary alloy.
290 Strong natural convection, however, results in substantial positive segregation at the center. This
291 reduces the contribution due to grain settling and leads to almost no segregation at the center. In the
292 end, shrinkage induced flow remains as the major contributer to negative segregation at the center
293 when all transport mechanisms are combined. A similar conclusion holds for the Al-Zn alloy. The
294 differences in the intensities of segregation between Cu and Zn can be attributed to the difference in
295 their partition coefficients[1].

5. Conclusions

299 A systematic qualitative study on impact of alloying elements on macrosegregation formation in an
300 industrial scale DC cast ingot is made. Three different binary alloys are chosen for this purpose – Al-
301 Mg, Al-Zn and Al-Cu. For the given casting conditions, it was seen that all three alloys exhibit similar
302 macrosegregation profiles when all the transport phenomena are considered simultaneously. Only
303 with the study of impact of individual transport mechanisms, the relative importance of each
304 phenomenon could be established.

306 Based on the presented analyses, the main difference between the considered Al-Mg, Al-Cu or Al-Zn
307 alloys lies in the role and intensity of natural convection. This difference invariably leads to different
308 transport phenomena contributing to negative segregation at the center. Shrinkage induced flow and
309 grain motion together contribute to negative segregation in the center for Al-Mg system. For Al-Cu
310 and Al-Zn, it is mainly due to shrinkage induced flow as the impact of grain motion negative
311 segregation at the center of ingot is reduced by co-operating thermal and solutal convection.

313 Note, however, that several simplifications have been introduced in the present work. The alloy
314 system can impact on grain growth kinetics and morphology evolution, which in turns can affect the
315 packing fraction also assumed constant in the present work. These can have an impact on grain
316 motion and the intensity of macrosegregation due to the interplay between natural convection and
317 grain motion.

319 In addition, based on the results from this work it becomes important to consider further
320 improvements in modelling transport in the packed porous portion of the mushy zone. The
321 permeability of the mush depends on the characteristic length size (l_{KC}) which is assumed constant.
322 This can change depending on grain morphology and grain diameter and this effect can be significant
323 close to the surface of the ingot where the impact of grain motion is minor. An improved estimation of
324 characteristic length size by considering its dependance on the grain structure needs to be included in
325 the model. Also, the work done in this paper uses simple binary alloys and it is worth investigating the
326 behavior of a system with multicomponent alloys.

6. References

335 1   R. Nadella, D.G. Eskin, Q. Du, and L. Katgerman: *Prog. Mater. Sci.*, 2008, vol. 53, pp. 421–

336   80.

337   2   A. V. Reddy and N.C. Beckermann: *Metall. Mater. Trans. B*, 1997, vol. 28, pp. 479–89.

338   3   J. Ni and C. Beckermann: *Metall. Trans. B---Process Metall.*, 1991, vol. 22, pp. 349–61.

339   4   C.Y. Wang and C. Beckermann: *Metall. Mater. Trans. A*, 1996, vol. 27A, pp. 2754–64.

340   5   C.Y. Wang and C. Beckermann: *Metall. Mater. Trans. A*, 1996, vol. 27A, pp. 2765–83.

341   6   C.J. Vreeman, M.J.M. Krane, and F.P. Incropera: *Int. J. Heat Mass Transf.*, 2000, vol. 43, pp.
342   677–86.

343   7   C.J. Vreeman and F.P. Incropera: *Int. J. Heat Mass Transf.*, 2000, vol. 43, pp. 687–704.

344   8   A. Ludwig and M. Wu: *Metall. Mater. Trans. A*, 2002, vol. 33, pp. 3673–83.

345   9   A. Ludwig and M. Wu: *Mater. Sci. Eng. A*, 2005, vol. 413–414, pp. 109–14.

346   10   M. Wu and A. Ludwig: *Metall. Mater. Trans. A Phys. Metall. Mater. Sci.*, 2007, vol. 38 A, pp.
347   1465–75.

348   11   M. Wu and A. Ludwig: *Acta Mater.*, 2009, vol. 57, pp. 5621–5631.

349   12   M. Založnik and H. Combeau: *Comput. Mater. Sci.*, 2010, vol. 48, pp. 1–10.

350   13   M. Wu, A. Fjeld, and A. Ludwig: *Comput. Mater. Sci.*, 2010, vol. 50, pp. 32–42.

351   14   K.O. Tveito, A. Pakanati, M.M. Hamdi, H. Combeau, and M. Založnik: *Metall. Mater. Trans.*
352   *A*, , DOI:10.1007/s11661-018-4632-1.

353   15   D.G. Eskin, Q. Du, and L. Katgerman: *Metall. Mater. Trans. A Phys. Metall. Mater. Sci.*,
354   2008, vol. 39 A, pp. 1206–12.

355   16   M. Založnik, A. Kumar, H. Combeau, M. Bedel, P. Jarry, and E. Waz: *Adv. Eng. Mater.*, 2011,
356   vol. 13, pp. 570–80.

357   17   M. Založnik, A. Kumar, H. Combeau, M. Bedel, P. Jarry, and E. Waz: *Essent. Readings Light*
358   *Met. Vol. 3, Cast Shop Alum. Prod.*, 2013, pp. 848–53.

359   18   M. Bedel: PhD Theses Université de Lorraine, Nancy,France, 2014.

360   19   L. Heyvaert: PhD Thesis, Université de Lorraine, Nancy, France, 2015.

361   20   M. Bedel, L. Heyvaert, M. Založnik, H. Combeau, D. Daloz, and G. Lesoult: *IOP Conf. Ser.*
362   *Mater. Sci. Eng.*, , DOI:10.1088/1757-899X/84/1/012100.

363   21   H. Combeau, M. Založnik, and M. Bedel: *Jom*, 2016, vol. 68, pp. 2198–206.

364   22   L. Heyvaert, M. Bedel, M. Založnik, and H. Combeau: *Metall. Mater. Trans. A*, 2017, vol. 48,
365   pp. 4713–34.

366   23   A. Pakanati, K.O. Tveito, M. M'Hamdi, H. Combeau, and M. Založnik: in *Light Metals 2018*,
367   2018, pp. 1089–96.

368   24   K.O. Tveito, M. Bedel, M. Založnik, H. Combeau, M. M'Hamdi, A. Kumar, and P. Dutta: *IOP*
369   *Conf. Ser. Mater. Sci. Eng.*, 2012, vol. 33, p. 012089.

370   25   T. Jalanti: PhD Thesis, Ecole Polytechnique Fédérale de Lausanne, Laussanne, Switzerland,
371   2000.

372   26   A.L. Greer, A.M. Bunn, A. Tronche, P. V. Evans, and D.J. Bristow: *Acta Mater.*, 2000, vol.
373   48, pp. 2823–35.

374   27   D. Weckman and P. Niessen: *Metall. Trans. B*, 1982, vol. 13, pp. 593–602.

375   28   A. Tronche: PhD Thesis, University of Cambridge, Cambridge, England, 2000.

376   29   H. Combeau, M. Založnik, S. Hans, and P.E. Richy: *Metall. Mater. Trans. B Process Metall.*
377   *Mater. Process. Sci.*, 2009, vol. 40, pp. 289–304.

378   30   T. Chandrashekar, M.K. Muralidhara, K.T. Kashyap, and P.R. Rao: *Int. J. Adv. Manuf.*
379   *Technol.*, 2009, vol. 40, pp. 234–41.

380   31   D.G. Eskin, J. Zuidema, V.I. Savran, and L. Katgerman: *Mater. Sci. Eng. A*, 2004, vol. 384, pp.
381   232–44.

382

383